LLNL-JRNL-840753

A Denoising Autoencoder for Improved Kikuchi Pattern Quality and Indexing in Electron Backscattered Diffraction

C. E. Andrews, M. Strantza, N. P. Calta, M. J. Matthews, M. L. Taheri

October 4, 2022

Ultramicroscopy

Disclaimer

Title: A Denoising Autoencoder for Improved Kikuchi Pattern Quality and Indexing in Electron Backscatter Diffraction

Authors: Caleb E. Andrews[A], Maria Strantza[B], Nicholas P. Calta[B], Manyalibo J. Matthews[B], Mitra L. Taheri[A*]

A: Johns Hopkins University, Department of Materials Science
B: Lawrence Livermore National Laboratory, Materials Science Division
*Corresponding Author: mtaheri4@jhu.edu

Abstract: The rapid collection and indexing of electron diffraction patterns as produced via electron backscatter diffraction (EBSD) has enabled crystallographic orientation and structural determination, as well as additional property-determining strain and dislocation density information with increasing speed, resolution, and efficiency. Pattern indexing quality is reliant on the noise of the collected electron diffraction patterns, which is often convoluted by sample preparation and data collection parameters. EBSD acquisition is sensitive to many factors and thus can result in low confidence index (CI), poor image quality (IQ), and improper minimization of fit, which can result in noisy datasets and misrepresent the microstructure. In an attempt to enable both higher speed EBSD data collection and enable greater orientation fit accuracy with noisy datasets, an image denoising autoencoder was implemented to improve pattern quality. We show that EBSD data processed through the autoencoder results in a higher CI, IQ, and a more accurate degree of fit. In addition, using denoised datasets in HR-EBSD cross correlative strain analysis can result in reduced phantom strain from erroneous calculations due to the increased indexing accuracy and improved correspondence between collected and simulated patterns.

Graphical Abstract:

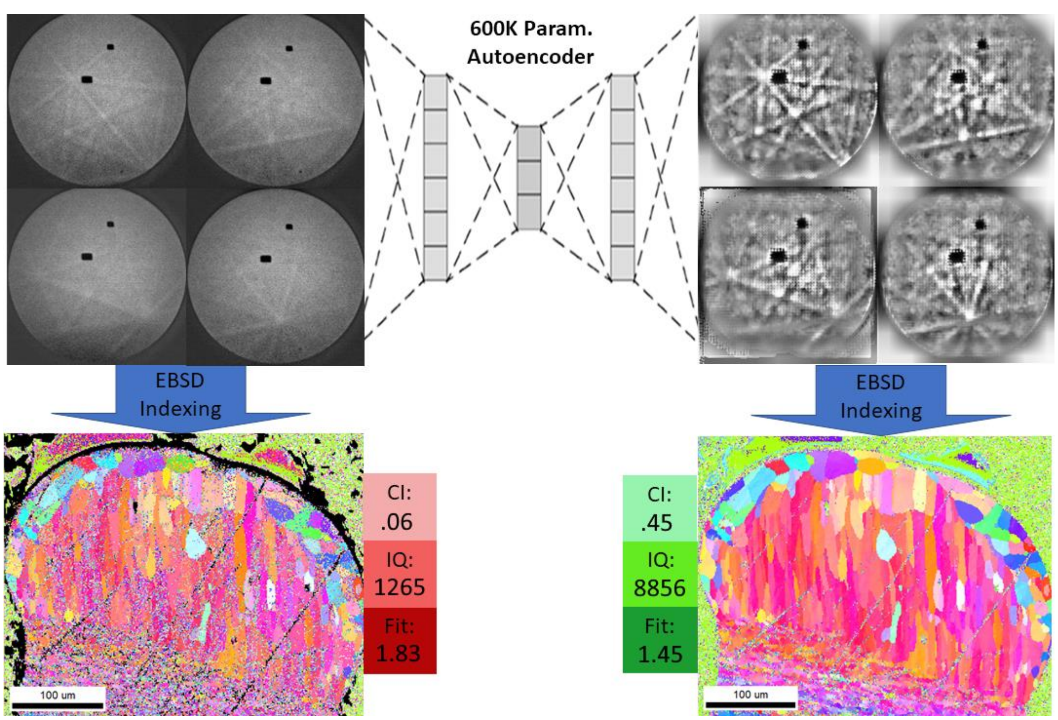

LLNL-JRNL-840753

1) Introduction:

Electron backscatter diffraction (EBSD) is of the most commonly used microstructural analysis tools, and is a widely accessible tool in the materials science and crystallography community. [1] EBSD enables users to obtain a wealth of information from crystalline materials in a conventional scanning electron microscope (SEM) that would traditionally require access to a beamline or similar X-ray techniques: such as crystallographic orientation, distribution of phases within a microstructure, dislocation defect density, and grain size and texture information. [2] In addition to the acquiring crystallographic information, the method enables the measurement of microscale strains in materials with a sensitivity of 10^{-4} through a process of electron backscatter diffraction pattern (EBSP) cross correlation, using high resolution electron backscatter diffraction (HR-EBSD). [3]–[5] Strain determination is accomplished by two different approaches and arrives at two different strain measurements. The first method of relative strain mapping calculates local strain gradients by measuring pattern shifts between two captured patterns, a reference and a test, experimentally this is often preformed such that the reference pattern is that of the grain mean orientation. [6], [7] However, the unknown strain state contained within the reference pattern carries with it uncertainty, and thus this method does not provide a true absolute strain measurement, only relative/deviatoric distortions between the reference and test pattern. [8] The second, more computationally complex method, dynamically simulates a strain free reference pattern for each experimentally obtained pattern and thus determines absolute strain at each point in an EBSD scan. [9], [10] Thus, obtaining an absolute strain measurement relies on the simulation of a ‘zero strain’ reference pattern which closely converges with the experimental one and is limited by two sources of uncertainty: the uncertainty of orientation measurement via Hough transform [1] and uncertainty of pattern center (PC) from conventional SEM calibration techniques which can introduce phantom strains on the order of 10^{-3}. [11], [12] Despite advances in improving correspondence between the simulated and real patterns through a gradient-based approach [13] there is still often insufficient correspondence between real and simulated patterns which introduce limitations to this method in obtaining an absolute strain measurement. [1], [14] Although many authors have reported and worked on solutions related to PC shift correction [8], [13], this paper focuses on improving the experimentally collected EBSPs, also known colloquially as Kikuchi patterns, themselves and achieving a higher accuracy measurement of orientation angles and enabling a higher resolution Hough transform indexing procedure and has implications beyond strain measurement.

All EBSD methods rely on the correct identification and indexing of bands appearing on the EBSP which represent the crystal lattice planes, determining the positioning and angles between these bands, and from this the orientation of the local crystal lattice can be measured. [15]–[17] The most commonly used method of indexing EBSPs utilizes band detection via Hough transform, whereby each Kikuchi line in detector space is a 2D point of accumulation (a peak of high intensity) in transform space. [18] Thus, in transform space the distance and angle between these peaks can be measured trivially and the relationship between the planes in detector space elucidated to determine crystallographic orientation. [15], [19] This method has been integrated into many commercial systems and has seen widespread use and improvement over the past several decades, however this algorithm's performance degrades with increasing noise input. The Hough transform method suffers from poor indexing, fit, and confidence index (CI) in EBSPs featuring increasingly high noise levels, with noise primarily manifesting as low pattern contrast, Gaussian noise, or lack of clear band definition. [2], [20], [21] This noise can originate from sample preparation, the detector, microscope, and camera settings utilized (i.e. poor exposure), localized strain/deformation within the sample area, and improper utilization of large step sizes with fine-grained materials. [22]–[24] Various indexing algorithms have been introduced which aim to address these issues, each introducing their own advantages and drawbacks. Spherical indexing methods utilize a forward model to generate a spherical master EBSP from which collected patterns are projected onto and correlated via a spherical harmonic transform (SHT), resulting in higher indexing quality with EBSPs that would be difficult to index with traditional Hough techniques. [25] The dictionary indexing method (DI) has demonstrated the ability to index samples with greater accuracy and correctly index patterns with high noise [24], [26], but the size of the simulated pattern dictionary increases with decreasing crystal symmetry; meaning that indexing a cubic material will take six times less computation time than indexing an orthorhombic one. [25] Computation time is the largest drawback of the DI method, with an indexing speed of ~12 points per second and larger datasets taking days to process when including orientation refinement. [27] For context, both the Hough method and SHT method are capable of processing hundreds to thousands of points per second and are limited more by EBSD detector speed and exposure settings than execution time. [25] Refinements and optimization to the DI method have been forwarded to improve execution time, with Fourier domain based pattern matching enabling more rapid orientation refinement and requiring a smaller pattern dictionary to parse. [28]

While introducing the subject of noise and its implications towards EBSD indexing, we must also briefly discuss the quantification of EBSD data quality metrics. Quality in an EBSD context can refer to two things, the quality of the diffraction pattern itself and the quality of the indexing solution of that pattern to a crystal system. Quality at the pattern level is a measurement of how well defined the Kikuchi bands are relative to the background, with higher quality patterns featuring bands of high intensity and sharp band edges. [29] This is often defined as image quality (IQ), a measure of the average height of the Kikuchi band peaks in Hough space, and is effected by local lattice strain, the atomic scattering factor of the material being analyzed, surface preparation and/or topology, and other microstructural features like grain boundaries which would result in low IQ. [30], [31] As indexing and/or SEM parameters will often induce changes to IQ irrespective of the microstructure, relative values between points are used to describe microstructural features and an absolute measure of IQ is not particularly useful in this regard. [30] Indexing success rate (ISR) is a general term for describing the fraction of patterns successfully indexed in an EBSD scan, and this is defined differently depending on the EBSD detector manufacturer. At time of writing Oxford and Bruker systems describe this as the fraction of zero solutions, or points with no indexing solution to the corresponding pattern, while EDAX systems utilize a triplet voting method, defined as a confidence index (CI), to provide a measure of how reliable the indexing solution would be on a scale of 0 to 1. [24], [32] A 'vote' in this context is an orientation solution for a set of Kikuchi band triplets, the more well fit that solution is the more votes it receives, and the CI is calculated as the difference in votes between the most likely solution (determined by number of votes) and the second most likely, divided by the number of total band triples available. [19], [32], [33] CI is impacted by the number of bands present in a pattern, with more bands resulting in a greater number of correct solutions, but a lower average CI due to conflicting votes; experimentally this results in ~90% of the orientation solutions being correct with a CI=0.1. [34] Degree of fit is another ISR metric, and defines the degree of angular deviation between the observed crystallographic orientation of the EBSP and the ideal solution provided by the indexing software. [35] There is no one single quality metric which can fully describe an EBSD dataset due to the physics of diffraction, for example a highly strained sample would result in lower IQ than a relaxed one but could still feature high ISR. In addition, different detector manufacturers will use different image collection, processing, and measurement methods all of which impact these metrics which is beyond the scope of this study.

Machine learning (ML) methods have been recently introduced as an alternative to the discussed algorithms as a method of indexing EBSPs. [36] Deep learning methods, such as the use of convolutional neural networks (CNNs) trained with simulated EBSPs, have indexed polycrystalline nickel with decreased disorientation error when compared to DI methods. [37] Refinements and improvements to the CNN indexing method, including EBSP preprocessing and use of disorientation error as its own loss function, resulted in a model fast enough for real-time indexing but performed slightly worse at indexing noisy patterns. [38] These improved indexing methods offer reduced orientation fit error over the conventional Hough methods, which is key for cross-correlative strain determination and accurate indexing of strained materials. [1], [37]

Image processing algorithms which aim to denoise the EBSPs themselves, rather than addressing noise at the indexing stage, have also shown utility. The commercially available Neighbor Pattern Averaging & Reindexing (NPAR™) algorithm averages neighboring patterns above a CI threshold, which has shown improved Hough indexing and enables the collection of data at higher speed with more noise. [24], [39] NPAR functions as a virtual pattern averaging function which can be done post-process, as it averages patterns across space it is inherently lossy with spatial resolution, and NPAR is less effective with larger step sized scans and fine grained materials. This method has been refined using a non-linear smoothing kernel (NLPAR) to weigh patterns based on their similarity of quality, rather than their spatial proximity, and results in further improved results including gains over the DI method. [22] These are inherently post-process methods, but demonstrates that when using the conventional Hough indexing method, the quality of orientation mapping and index success rate can be improved through EBSP preprocessing and denoising.

Utilizing a denoising autoencoder (DA) approach to preprocess EBSPs prior to indexing should lead to indexing improvement, without needing to alter the indexing process itself. Autoencoders are a type of feedforward neural network model consisting of two functions: an encoder which translates the input into latent space, and decoder, which attempts to reconstruct the input from this latent space representation. [40] The goal of a DA model is to learn to reconstruct a noise-free output from a noisy input. [41] Using DAs for image denoising has shown utility in removing Gaussian noise and undesired features from image data. [42] Stacked convolutional

DAs have been able to denoise medical mammogram and X-ray images with very small training datasets, and reconstruct images from incredibly noisy datasets. [43], [44] Thus, there is evidence that utilizing DAs at the stage of EBSP collection or prior to indexing could reduce noise within the EBSPs themselves which would result in erroneous or poor indexing.

In this paper, by synthesizing both ML and conventional image processing methods, we introduce a convolutional DA framework for EBSD denoising which has shown to significantly improve indexability of poor quality EBSPs and improve the fit accuracy of the Hough transform method with DA-processed patterns. By addressing noise at the EBSP level, we are able to improve the CI, image quality (IQ), and degree of fit both among individually noisy patterns and across the whole dataset. In addition, this DA framework reduced the contributions of 'phantom strain' in dynamically resolved absolute HR-EBSD strain measurement because of this improved fit accuracy. By improving the pattern quality and Kikuchi band edge fidelity, the accuracy of interplanar angle measurement of the Hough indexing procedure was improved. Because of this we observe increased correspondence between experimental EBSPs and simulated ones used for strain cross correlation. EBSPs denoised by the autoencoder often demonstrate a sub-1° of fit, with indexing metrics showing improvement over and compatibility with existing EBSP image post-processing methods. In addition to improving HR-EBSD absolute strain determination, this allows for noisier EBSD datasets to be collected and indexed with conventional Hough-based indexing and thus enables higher speed and higher resolution EBSD experiments in general.

2) Sample Preparation and EBSP Acquisition Methods:

Two HR-EBSD datasets were utilized to build and demonstrate the DA, both captured from the cross-sectional surface of a Ti-5553 melt bead. First, an 'ideal' EBSD dataset was taken from a well-polished, scratch free, surface captured using 4x frame averaging resulting in slow capture rates but high quality orientation data; the EBSPs from this dataset would ultimately not be used in any following analysis, but the orientation data from this scan would be used to generate and simulate patterns for DA training. These Ti-5553 surfaces were then heat treated to relieve any internal residual stresses in a Across TF1700 tube furnace at 300°C for 2 hours and allowed to cool at 2 °C/min under .5L/min of argon to prevent oxidation. We then collected a second, demonstrative, HR-EBSD dataset from a scratched, poorly prepared, surface. This dataset was chosen specifically because of the presence of multiple surface defects, lackluster pattern quality, poor indexing metrics, and represents the experimental "as-collected" data being denoised and reindexed. Both of these HR-EBSD datasets were collected on a ThermoFisher G4 UC DualBeam FIB/SEM equipped with an EDAX Velocity EBSD camera, while the resulting data from the "as-collected" surface was indexed with TSL OIM Analysis Version 8.1. 2x2 binning was used on the detector representing a EBSP resolution of 235x235 pixels. Note that our detector featured two dead zones along the phosphor screen, these are present visually as two dark rounded rectangles in the EBSPs shown in Figures 2 and 3. These dead zones were caused by a sample crash from a prior user, and served to demonstrate a 'worst case' scenario of detector damage induced noise on pattern collection. Collected data was then processed through the DA and reindexed in TSL OIM Analysis software to understand the effects of EBSP denoising on indexing metrics. Model training and the theory behind that training is described in section 3.1.

Seeking to extend the improvements from indexing towards HR-EBSD dynamic strain measurements, the original as-collected data and DA-processed reindexed data was analyzed using the open source EBSD cross correlation software OpenXY. [45] Dynamically simulated reference patterns were used in cross-correlation utilizing the EMSoft method described in section 3.1 and 3.2. Mutual image information between simulated, zero-strain, EBSPs and the experimental, as-collected, EBSPs was calculated with each iteration of cross-correlation for both input datasets. No pattern centering (PC) calibration was performed in OpenXY, and a radial region of interest (ROI) pattern was utilized with a total of 48 ROI's across each EBSP being utilized in the shift calculations which is described in section 3.2.

3) Theory and Calculation:

3.1) Dataset Generation and Training the Denoising Autoencoder

To generate EBSPs to train the model, a representative noise free dataset was generated using the Monte Carlo-based EBSP simulation suite, EMSoft [46], from the crystallographic orientation information from the 'ideal' EBSD dataset mentioned in the Methods section. First, an EBSP master pattern file was generated for β-titanium matching the energy conditions used in the microscope. This method uses the Bethe Continuous Slowing Down Approximation implemented in Fortran, along with the scattering cross sections determined by Rutherford scattering, to produce distributions of the depth, direction, and energy of billions of back-scattered electrons (BSEs) as reflected from a simulated β-titanium surface to produce simulated EBSPs from these reflection conditions. [47] Using the Euler orientation data from the first 'ideal' dataset, the microscope conditions/geometry, and the simulated electron diffraction distributions, 37,135 simulated EBSPs were generated to construct a training dataset of noise free simulated EBSPs. A matching noisy dataset was then constructed from these simulated EBSPs, artificially noised with Gaussian noise ($\mu=0$, $\sigma=25$) and their contrast levels reduced in imageJ to closely resemble low contrast found in the as-collected experimental EBSPs. Thus, the autoencoder is trained via simulated EBSPs entirely and learns to reduce noise and enhance contrast to what an idealized EBSP should look like regardless of orientation, crystal system, or indexing solution. The autoencoder was programmed in Python utilizing the TensorFlow libraries and trained with the simulated images. The model was trained for 10 epochs, a batch size of 64, utilizing the 'adam' optimizer, and the mean square error loss function; resulting in a final loss value of .0022. TensorFlow was not compiled or optimized for GPU utilization, and all code was run on the CPU of a commercially available workstation. After training, the model was validated with the simulated EBSPs such that the DA was able to accurately reconstruct noise-free output from noise-free input as well as denoised output from noisy input. A schematic of this process and where the DA fits in the HR-EBSD indexing procedure is described in Figure 1, while a more in-depth flowchart of the autoencoder network and workflow is given in the supplemental. The code utilized, the autoencoder model, and its weights are available at the sourced Github. [48] A figure describing the training workflow, the architecture of the autoencoder, and the denoising workflow is shown visually in the Supplemental Figure S1.

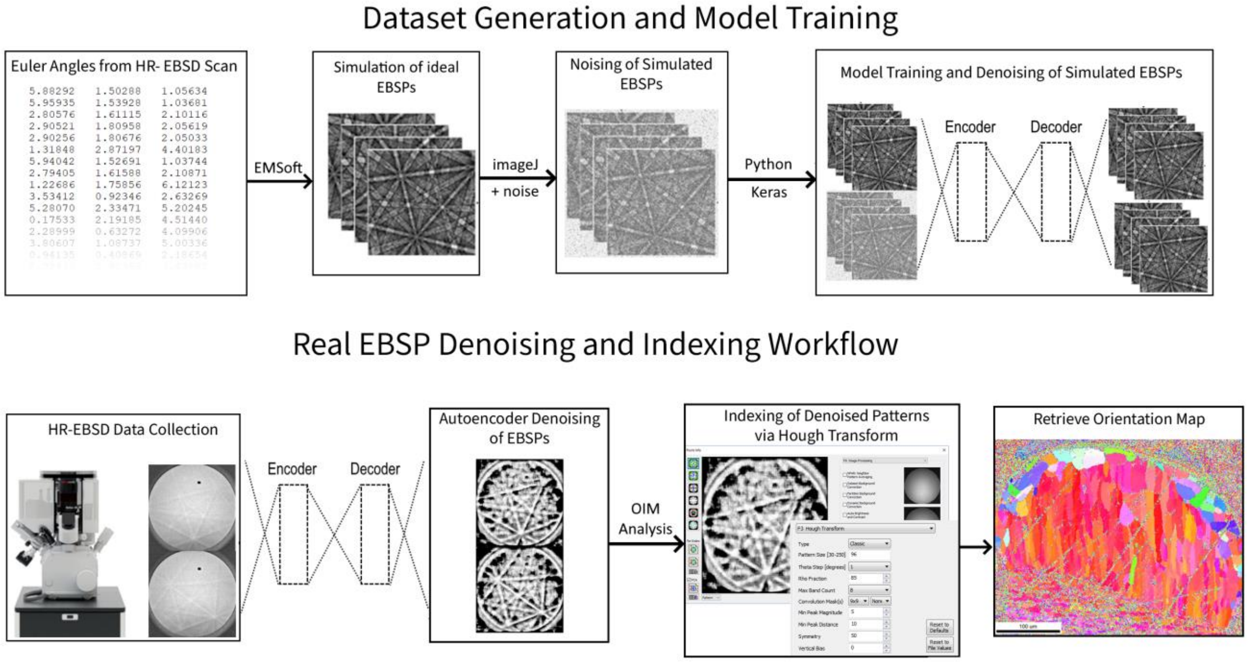

Figure 1: General workflow describing the autoencoder training methodology and its use within the EBSD indexing procedure.

3.2) Denoising, Re-indexing Patterns, and Strain Cross Correlation

The noisy, as-collected, experimental EBSPs from the heat treated surface were stored in the proprietary EDAX *.up2* format, a single file storing every EBSPs in the scan as a 16-bit unsigned binary file with a mixed bit-depth header. This raw image file was separated into individual files such that the model could encode/decode each individual image rather than loading the entire image dataset into memory, or needing to build a method to parse the large proprietary datafile. Each EBSP was then processed through the trained DA using Keras' forward prediction functionality. Optional in this process is the use of contrast limited adaptive histogram equalization (CLAHE) as implemented in the CV2 library for either pre-processing or post-processing of EBSPs alongside DA-processing, and in this case CLAHE was applied post-DA-process to produce the results shown in section 4. The directory of loose images is then repackaged into the *.up2* format for analysis and re-indexing in TSL OIM Analysis v8. Dataset background correction and/or automatic brightness and contrast (auto B/C) was utilized when re-indexing to examine how the DA-processed EBSPs could be further enhanced by common image processing methods and how they compare with them. The same methods were utilized on both the as-collected patterns and DA-processed patterns to allow a direct comparison.

Quantifying residual strain in the datasets was performed with the open-source software package OpenXY [45], utilizing the dynamically simulated pattern configuration for absolute strain determination. Specifically, the stable 'UPfile' branch of OpenXY was utilized as it gives the ability to load and quickly work with the *.up2* file format. The absolute cross-correlation process dynamically simulates an ideal, strain-free, reference EBSP through EMSoft for each orientation point and EBSP in the experimental datasets. At each point of cross-correlation an ROI screen is then applied to both the reference and experimental pattern, and the shifts in EBSP features within those ROIs is utilized to calculate the elastic distortion tensor: $\beta=F-I$. The full deformation gradient tensor, $F=R*U$, is split into a rotational (R) and strain (U) component, with the strain component given by $U=I+\varepsilon$. Thus, by comparing shifts between experimental and dynamically simulated strain-free reference patterns, the deformation gradient tensor and absolute strain within the experimental pattern can be determined by solving $F=R*U$ from the measured shifts in the elastic distortion tensor β and the identity matrix I. [8], [45], [49]

A detailed workflow showing all the steps utilized in EBSD data capture, image processing, indexing/re-indexing, EBSD data cleaning, and where the DA fits within this workflow is given in the Supplemental Figure S2.

4) Results:

4.1) Pattern Quality and EBSD Indexing Improvement

The model trained on simulated datasets was able to correctly identify that band contrast and Kikuchi line intersections were of visual importance, leading to local enhancement of the Kikuchi lines relative to the background, and resulting in more easily identifiable and pronounced peaks in Hough space. This is clear in Figure 2, which shows the IPF map of the as-collected EBSD data in contrast to the IPF map of the DA-processed data with examples of their respective EBSPs in real and Hough space. The denoised EBSPs show greater peak contrast in Hough space, and as a result the OIM Hough transformation and indexing algorithm produces a higher fit accuracy and confidence index. A full comparison of image processing and reindexing parameters between the as-collected and denoised EBSPs across the entire sample area is shown in Figures 4 and 5, with IQ, IPF, and fit maps given, and a table of indexing quality metrics shown in Table 2 to more quantitatively compare results with different re-indexing parameters. The total time for the model to load and denoise the entire dataset (124658 EBSPs) utilizing only the CPU was 3 hours and 19 minutes, translating roughly to a post-processing latency of 10.4 patterns/second.

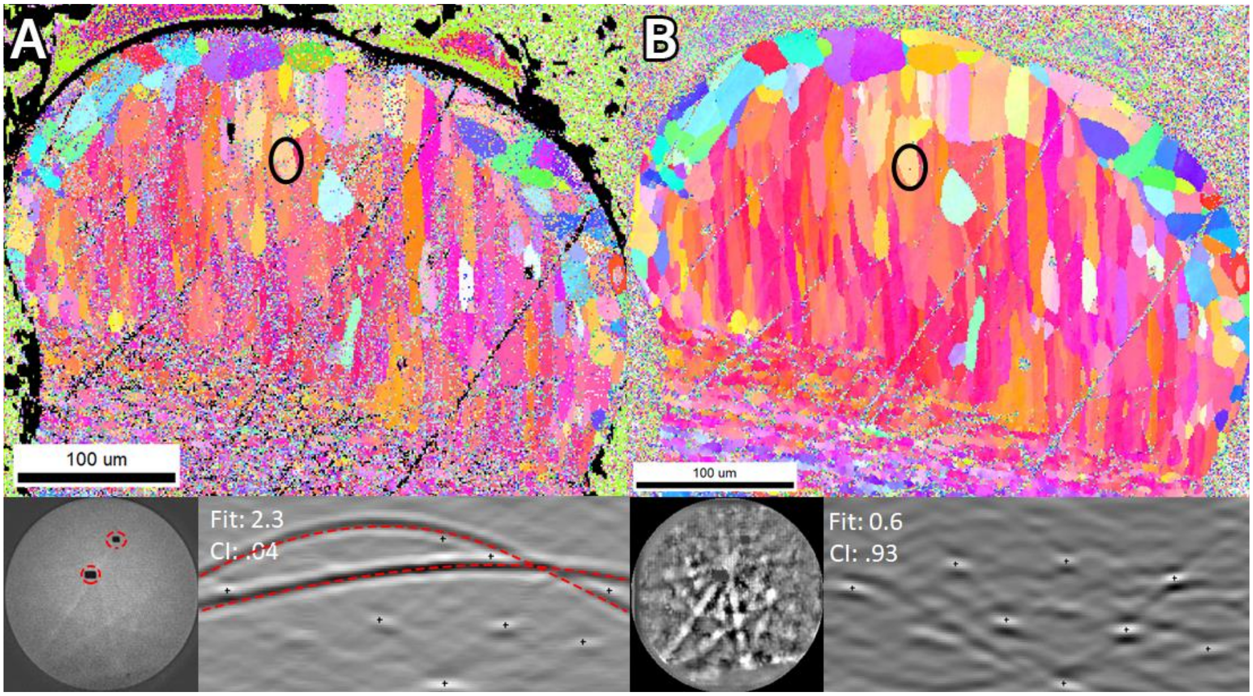

Figure 2: IPF map of the indexed as-collected EBSPs (A) and the DA-processed EBSPs (B), with respective EBSPs and resulting Hough transformation from a single point within the circled grain. The indexed fit and CI are given for each pattern, while detector dead zones are highlighted in both real and Hough transform space.

Figure 2 summarizes the overall improvements to indexing that patterns denoised with the autoencoder provided, showing the effect the autoencoder had on the EBSPs, their resulting Hough transformation, and improvement towards CI and degree of fit. Figure 2.A shows the IPF from the as-collected data without any further post-processing or re-indexing, with significant orientation noise visible within the scan. Figure 2.B shows the IPF generated by indexing the DA-processed EBSPs with background correction and auto B/C enabled as image processing during reindexing, it is identical to Figure 5.F. This highlights the best performing dataset, patterns which have been DA-processed and conventional image processed, alongside the worst performing dataset, the raw as-collected data. It is shown enlarged here for context to highlight how improvements to individual EBSPs processed by the DA result in an overall the reduction of noise visible in the orientation map. Note the effect of background correction on the dead zones highlighted in 2.A, and how these dead zones impact the quality of the initial Hough transform solution in comparison.

Examining the changes that both the autoencoder and conventional image processing techniques have on the diffraction patterns themselves, both in comparison and in combination, Figure 3 shows a cropped selection of the microstructures shown in Figure 2 and two diffraction patterns from the same grain for both the DA-processed patterns and the as collected patterns. The as-collected patterns and DA-processed patterns are shown both independently, and in combination with the common image processing options often used in post-collection re-indexing; the effects of which we show quantitatively in Table 2. There are distinct differences in the contrast and band definition when comparing the as-collected and DA-processed patterns, and differences in how these image processing options impact the final image quality of each. Background correction in both cases leads to the infilling and correction of the effects of the detector dead zone. It is not the DA-process which infills this detector damage noise, however there is less observable Gaussian-type noise introduced via background correction to the DA-processed patterns than the as-collected ones. In general, the definition of the Kikuchi lines and their intersection points are better defined against the background when comparing the DA-processed patterns to the as-collected patterns.

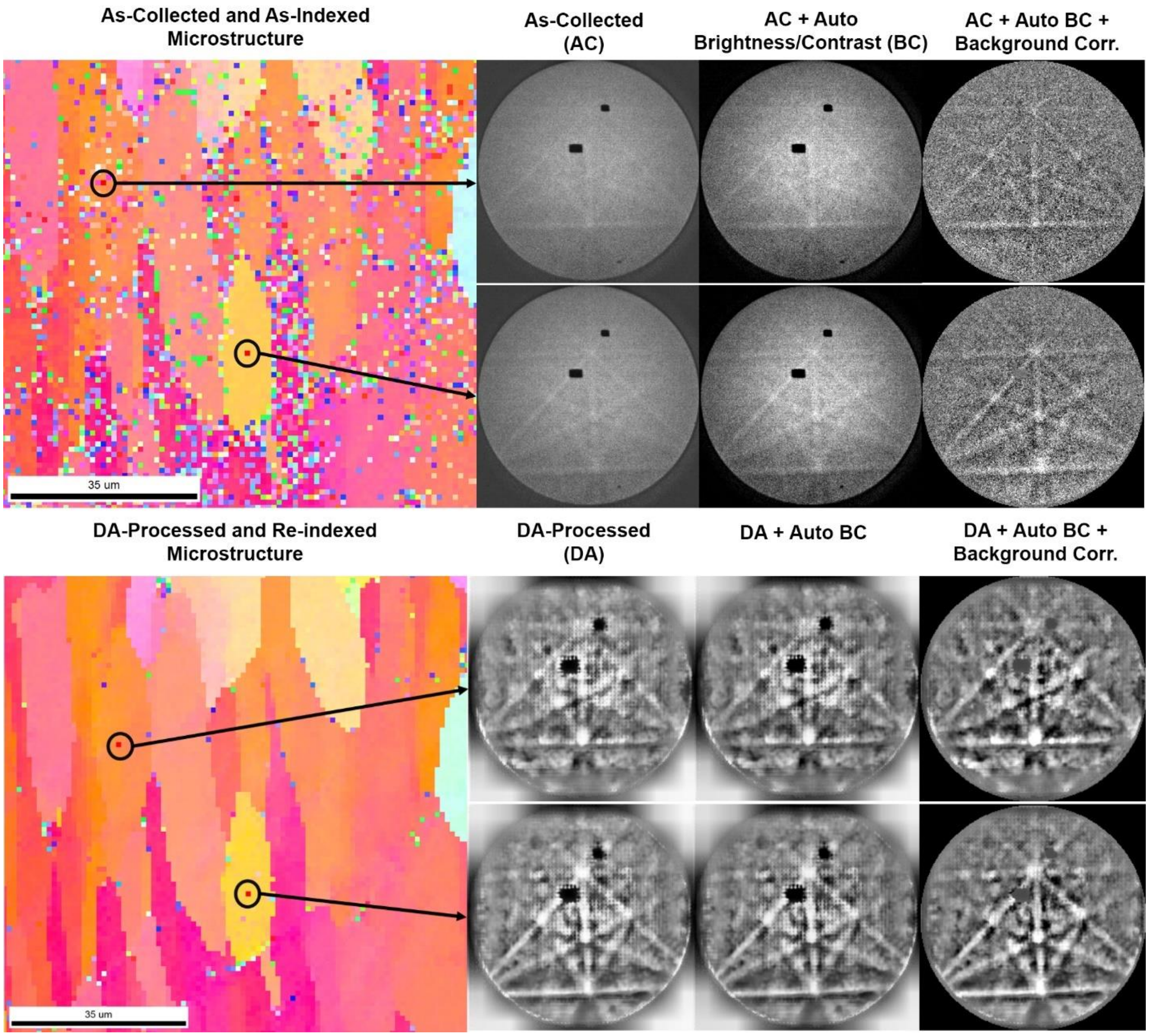

Figure 3: Pattern level comparison of DA-processing and common image processing techniques utilized in re-indexing.

Examining the IQ maps of each of these conditions in greater detail, the improvements shown at the pattern level can be observed across the whole microstructure dataset. Figure 4 shows the IQ maps of the same image processing conditions shown in Figure 3, allowing a comparison of IQ improvements between both conventional image processing and novel DA-processing pathways. Although improvements to IQ can be observed with the as-collected patterns using conventional image processing techniques, greater improvements to IQ are obtained through DA-processing, and these increases are further improved by subsequent image processing while reindexing. Note that scratches and pores remain relatively low in IQ as no diffraction would be expected in these regions.

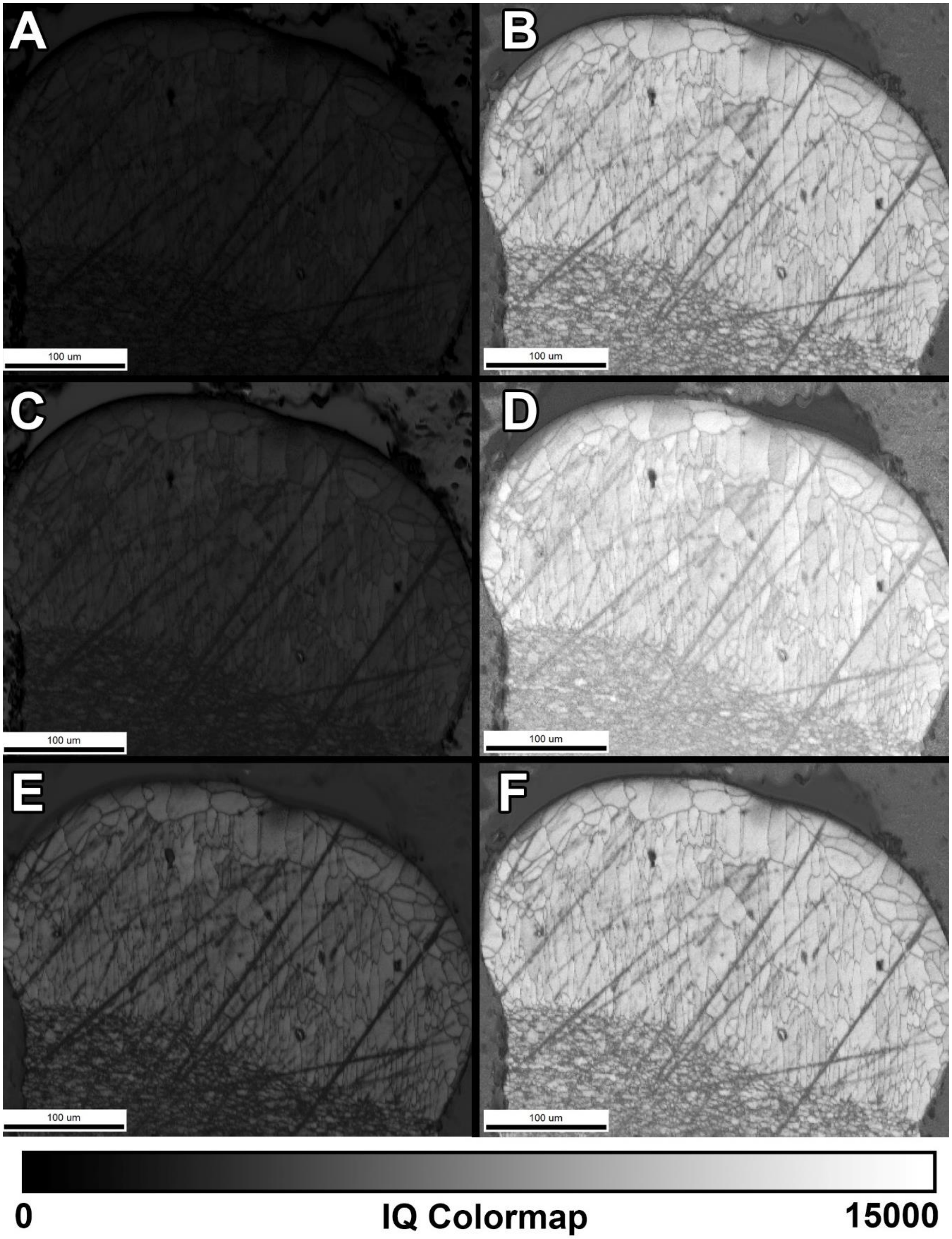

Figure 4: IQ maps of the EBSD dataset utilizing the as-collected patterns (A, C, E) and the DA-processed patterns (B, D, F). The IQ maps for both of these datasets re-indexed with automatic brightness and contrast enhancement are shown in (C) and (D), respectively, with the addition of background correction shown in (E) and (F).

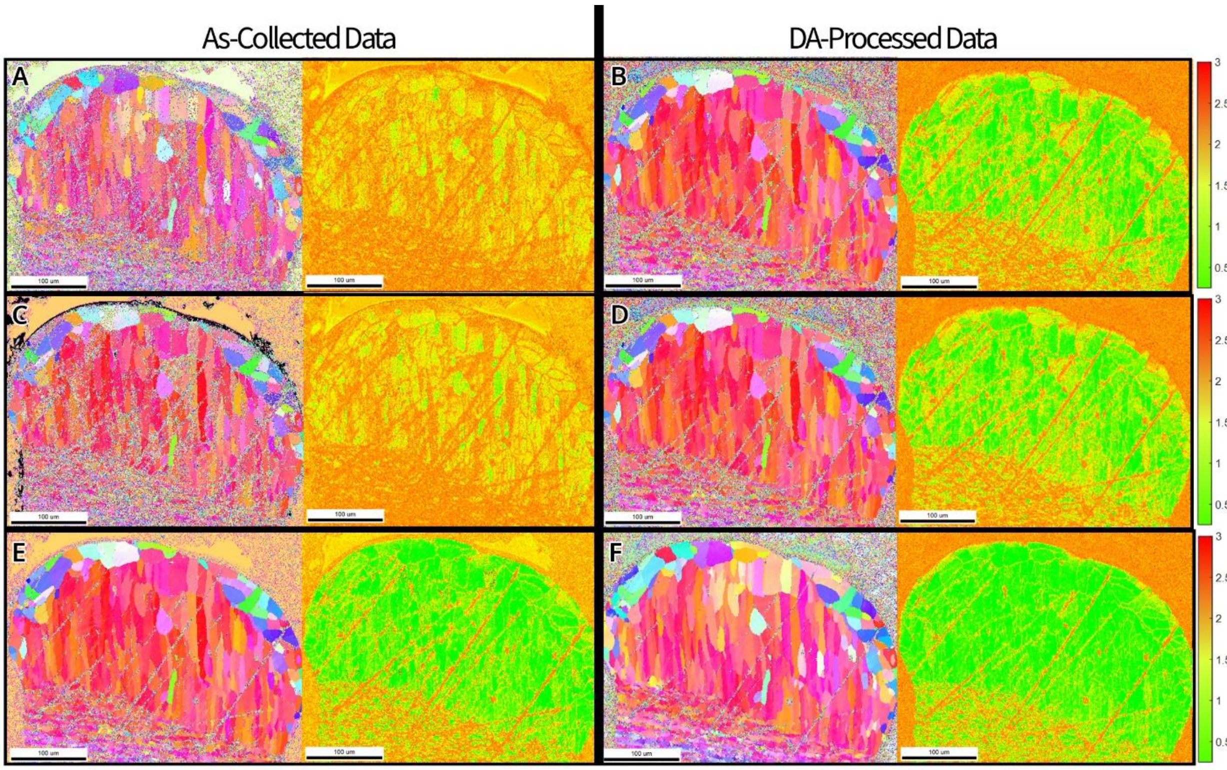

Figure 5: IPF (left) and degree of fit (right) maps of the as-collected and DA-processed datasets, with no additional image processing performed in re-indexing (A,B), with auto B/C adjustment preformed while re-indexing (C,D), and both auto B/C and dataset background correction preformed while re-indexing (E,F). The scalebar reads 100µm.

Figure 5 visually demonstrates the denoising performance of the EBSPs processed through the autoencoder (B,D,F) with the as-collected EBSPs (A,C,E) combined with commonly used EBSD post-processing techniques used in re-indexing: auto B/C and background noise correction. Figure 5.C shows that auto B/C alone is insufficient, showing minimal improvements to fit accuracy and orientation noise, while Figure 5.E indicates that incorporating background correction in re-indexing alongside auto B/C can improve fit and indexing quality, but is outperformed by the DA when combined with the same image processing conditions as shown in Figure 5.F. The DA-processed data shown in Figure 5.B resulted in significantly less orientation noise and a higher degree of fit accuracy when indexed compared to the as-collected patterns, both with and without auto B/C image processing shown in Figure 5.C and 5.A respectively. Combining the DA-processed patterns with a combination of image processing while re-indexing resulted in the best performance, with superior indexing metrics shown for all DA-processed data relative to as-collected data, resulted in higher IQ in all cases, reduced orientation noise, and significantly improved indexing properties when quantitatively compared in Table 2.

Table 2: Comparison of indexing metrics between the as-collected (AC) EBSPs and DA-processed EBSPs with common re-indexing post-processing settings: automatic brightness and contrast correction (auto B/C) and dataset background correction (back. corr.)

	As Collected (AC)	DA Processed (DA)	AC + auto B/C	DA + auto B/C	AC + auto B/C + back. corr.	DA + auto B/C + back. corr.
Average CI:	0.06	0.25	0.04	0.27	0.37	0.45
CI > .2 [%]:	5.29	42.85	7.86	45.02	54.18	62.30
Average Fit (°):	1.83	1.68	1.96	1.64	1.50	1.40
Fit < 1° [%]:	0.03	9.27	0.1	23.73	19.28	36.44
Average IQ:	1265	9804.54	2145	9682	3130	8856

The DA framework for denoising EBSPs resulted in higher CIs, fit, and IQ than the as-collected patterns when normalized across the different re-indexing image processing conditions, outperformed auto B/C image processing alone, and combing the DA with re-indexing image processing resulted in the best indexing performance. Although improvements can be observed with the as-collected EBSPs enhanced by combining both auto B/C and dataset background correction, it is important to note that these gains are only further enhanced through the use of the DA to process the EBSPs prior to re-indexing and that the DA results in significant improvements to fit, IQ, and CI on its own. Examining the CI distributions in greater detail, we find that the autoencoder results in high CI points with greater frequency than just using post-processing and re-indexing alone, and that the DA is not falsely generating indexable features from pure noise. This is clear when visualizing the CI as shown in Figure 6, in that regions we'd expect to be indexed with zero confidence (i.e. scratches, mounting compound surrounding the melt bead, and surface defects) are not artificially improved simply by parsing the patterns through the DA, and the CIs in these regions remains low. Instead, the DA results in increased frequency of high CI points (CI >.5) and reduced frequency of low CI points (CI < .2) compared to the as-collected data both with and without post-process re-indexing. Examining the CI distribution leads to a similar result described in Figure 5 and Table 2, where the DA-processed data shows large improvements over the as-collected data, and is further enhanced by using dataset background correction as image post-processing in re-indexing.

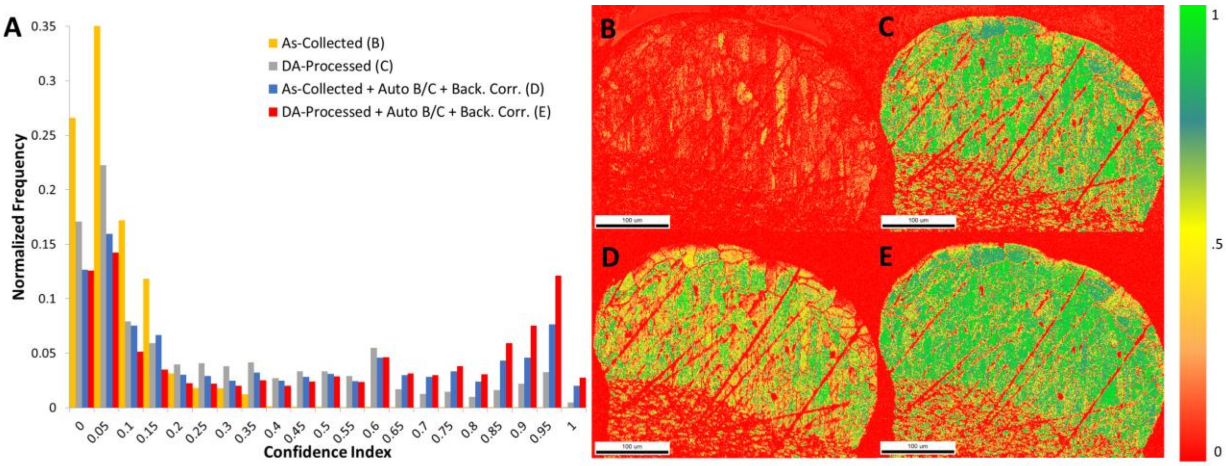

Figure 6: A comparison of CI values from indexed EBSPs as shown via histogram (A) and visually with a colormap. The CI maps from the as-collected data is shown in (B) while DA-processed data is shown in (C). Examining the effect of image processing while re-indexing, the CI maps for the as-collected (D) and DA-processed (E) EBSPs re-indexed with additional post-processing is shown in (D) and (E), respectively.

4.2) Autoencoder Denoising and Dynamic Strain Cross-Correlation

Generally speaking, two inputs are required in the dynamic cross-correlative strain measurement process: the experimental EBSPs which contain the local strain and orientation information and the corresponding map of indexed Euler angles. Examining how improvements to the EBSP pattern quality driven by the DA would impact the dynamic strain cross-correlation process, we find that the mutual information within the cross correlated regions of interest (ROI) is higher between DA-processed EBSPs and the simulated zero strain EBSP than with the as-collected EBSPs. Mutual information between two images is defined as the difference of the signal entropy between the two, normalized by the sum of their frequency histograms; in other words the DA-processed EBSPs feature greater ROI correspondence to and image likeness with simulated EBSPs when compared to as-collected EBSPs. [50] The distribution of the mutual information across the datasets is shown in Figure 6.A, showing the shift of the distribution to higher mutual information with the DA-processed EBSPs and DA-reindexed Euler angles. Examining if simply improving the degree of fit and providing more accurate Euler angle input to the cross-correlation process would result in more accurate strain measurement, Figure 7.B shows the resulting strain map when using the as-collected EBSPs but the DA-reindexed Euler angles for generating the simulated patterns. Better fit Euler angles combined with as-collected EBSPs results a noisy strain map with an order of magnitude of higher strain that does not trend with the other datasets, indicative of a poor absolute cross-correlation result. The strain maps using as-collected EBSPs and as-indexed Euler angles is shown in Figure 7.C, while the strain maps using the DA-processed EBSPs and DA-reindexed Euler angles is shown in Figure 7.D. The strain results indicate that using both the DA-processed images and the DA-reindexed Euler angles as cross-correlation input results in the clearest strain map, with reasonably low strain values for an annealed sample, and higher correspondence between the experimental pattern and the simulated one.

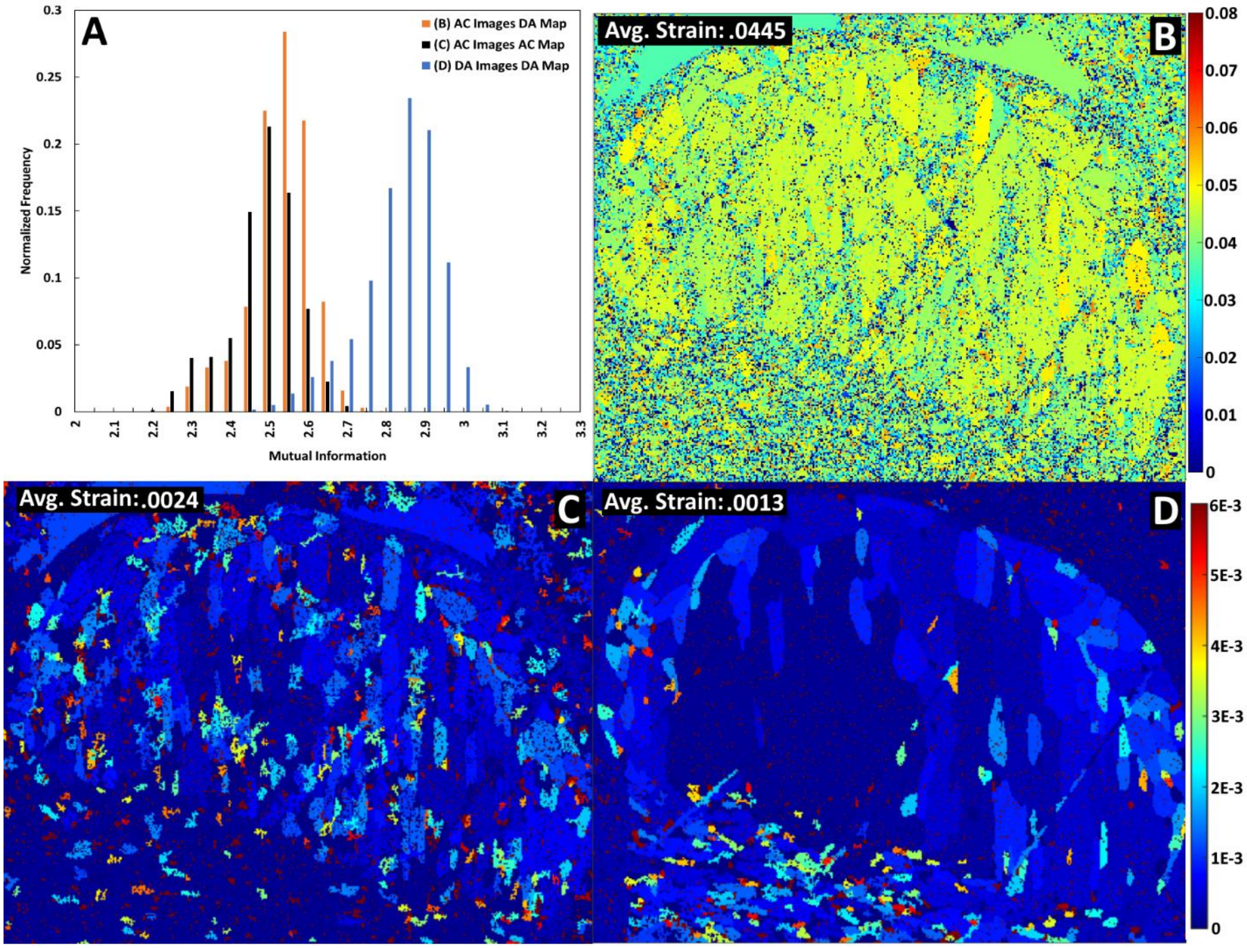

Figure 7: Histogram (A) of the mutual information between the experimental and simulated patterns used in HR-EBSD cross correlation, each distribution matching the dynamic strain analysis shown in the following plot. (B) shows the strain that results when correlating the as-collected patterns to patterns simulated using the Euler angles from the DA-reindexed fit, (C) is the strain resulting from as-collected patterns and the originally indexed Euler angles, and (D) shows the strain resulting from the DA-processed images correlated against patterns simulated from the DA-reindexed fit.

Further analyzing the mechanisms of how the EBSPs impact the dynamic pattern simulation and cross correlation process at the individual pattern generation and deformation gradient calculation level, Figure 8 shows the same two indexed EBSPs from the DA-processed and as-collected datasets alongside the simulated zero-strain EBSPs generated for both. The simulated EBSPs are overlayed with the ROI shift required to fit the two patterns, the magnitude of these shifts is used to calculate the deformation gradient tensor and thus strain between the zero-strain simulated reference and strained experimental EBSP. Figure 8 shows that the DA-processed images and better fit DA-reindexed Euler orientation results in a simulated EBSP with greater convergence with the experimental pattern, reduced local strains, and less computational iteration required to arrive at a solution. The simulated EBSP generated from the DA-processed orientation data more closely correspond to the experimental EBSP, and although subtle, this results in less rotational and positional deviation from the experimental pattern when compared to the as-collected dataset. Comparing the overlayed ROI shifts, the magnitude of these shifts is reduced when using the DA-processed data while the number of outliers is also reduced.

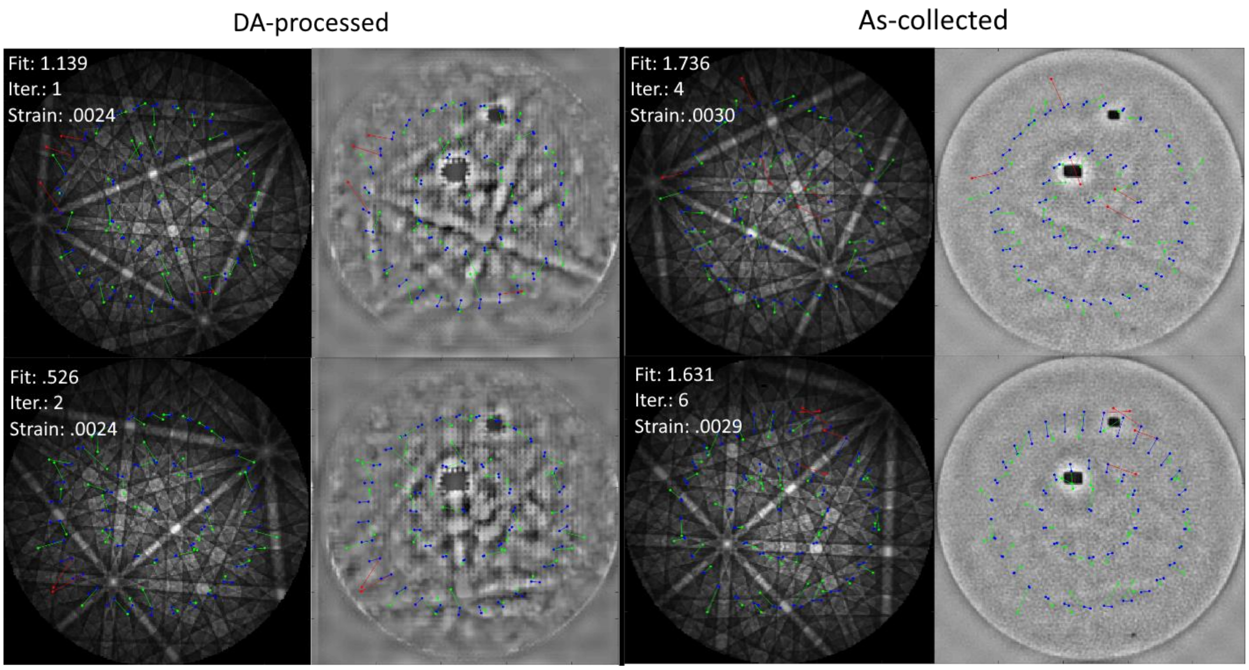

Figure 8: Comparison of the cross correlated ROI shifts between the simulated and experimental EBSP when using DA-process (left) and the as-collected and originally indexed data (right) from the same two points. Experimental EBSPs are shown to the right of their matching simulated EBSP. Annotated above each pair is the degree of fit, strain, and number of iterations required to arrive at the solution. The EBSPs are overlayed with ROI shifts: the green lines represent the shifts used to calculate the deformation tensor, red lines represent outliers ignored by the calculation, and blue lines are the shifts predicted by the final deformation gradient tensor.

5) Discussion

5.1) Improvements to EBSD Orientation Indexing

Utilization of a denoising autoencoder as an image preprocessor for EBSPs prior to indexing is a good solution for indexing noisy EBSD datasets, and especially when used in tandem with existing image processing like background correction and auto B/C, as usage of the autoencoder leads to a higher accuracy Hough indexing procedure than simply re-indexing with these options alone. Table 2 shows commonly described indexing metrics used to qualify EBSD scans (IQ, CI, fit), while Figure 2 and 3 describes at the pattern level the mechanism by which these improvements are derived. The accuracy of the Hough procedure, whereby the orientation of the crystal is determined by the angle and distance between the Hough peaks, rapidly deteriorates with image noise and especially band contrast. This lack of contrast results in low IQ, visible in the as-collected datasets in Figure 4. The low band contrast results in the Hough peaks shown in Figure 2.A being difficult to detect from the background, and are even skewed or overshadowed by a dead zone in the detector screen. In Figure 2.B we see that the autoencoder is able to enhance band contrast in the EBSPs and thus peaks in Hough space, and when combined with background correction also leads to infilling of dead zones on the detector. The improvements to band contrast across the whole dataset becomes clear when comparing the IQ maps in Figure 4, as the IQ of the whole dataset is improved, while relative differences in IQ values between grains are still maintained. These improvements are derived from how the model was trained. The simulated EBSPs generated by EMSoft contained no noise and perfect band contrast, and served as the training target. By artificially noising them to near-experimental levels and using this as the noisy training input, the autoencoder learns to reproduce high quality EBSPs from noisy ones. Although one single metric (IQ, CI, or fit) alone cannot alone describe the quality of an EBSD dataset due to the convolution of factors which cause noise in electron diffraction patterns, usage of a convolutional autoencoder leads to improvements to all metrics simultaneously. When utilized on noisy experimental patterns the model results in both visual and quantitative improvements to the IPF and degree of angular fit maps in Figures 5 while also improving the whole distribution of CI across the dataset as shown in Figure 6. Thus, the DA model improves both the fit of the orientation solution and the confidence in the accuracy of that solution simultaneously. Importantly, the degree of fit is improved with utilization of the DA prior to re-indexing, with Table 2 showing that ~36% of the data had a fit parameter of less than 1° of misorientation from the indexing solution. The improvements made using denoised EBSPs prior to Hough indexing results in orientation maps of similar quality to those demonstrated with the DI and SHT based indexing methods when indexing noisy datasets, but we note a full quantitative comparison between different indexing methods would require additional analysis as we are using an entirely different dataset and material system. [25], [51]

This denoising model is an inherently generative one, so it is critical we ensure the DA is not generating new information from pure noise or encoding new Kikuchi bands and EBSP features from non-existent data. The fit and CI values as mapped in Figures 5 and 6 are critical in assessing this. Scratches, defects, or a high density of grain boundaries on the imaged surface would result in EBSPs of high noise due to lack of coherent diffraction and would result in near zero CI and low fit accuracy within these regions. In the noisy as-collected dataset we see this is true, and the scratches stand out as a consistent low point of reference on the fit and CI maps of each dataset regardless of DA processing. Thus, we find that the DA is only improving EBSP features that are present, within regions where electron diffraction would be expected and observed. Regions of pure noise, such as those within the mounting compound, are not being falsely improved nor is non-existent data is being generated by the model as we do not see an indexing solution in these areas. Indeed, examining Figure 6 we find that denoising leads to improvement in CI within grains that were mapped with low confidence, rather than defects mapped with zero, and we observe that the DA results in an increase in frequency of high confidence points only within the melt pool boundary.

The noise limitations of the Hough transformation indexing procedure can be addressed by denoising the EBSPs prior to the transform as a form of image pre-processing, and a higher degree of angular fit, CI, IQ achieved while still using the conventional Hough indexing method. Because this denoising occurs post-collection, no additional processing time or latency is introduced at the point of data collection while still utilizing faster and more conventional Hough indexing once the EBSPs have been denoised, enabling more noise tolerant collection at the detector without additional time penalties induced by frame averaging or conventional image processing. The indexing uncertainties of the Hough-transform that arise from noisy images can be alleviated, and the autoencoder method of denoising we demonstrate shows greater robustness to pattern noise than convolutional neural network based indexing methods. [38] The DA method demonstrated offers improvements over the Hough-transform augmented with various forms of image post-processing, without the losses in resolution associated with NPAR. [24] The latency of the DA, running only on the CPU on a modest workstation (Intel i9-9900, 64GB RAM), is ~10.4 patterns/second and is comparable to that of the dictionary method at ~11.6 patterns/second. [27] The total calculation time from denoising to indexed solution is less, taking approximately 4 hours to denoise and reindex a dataset of 124658 EBSPs, compared to approximately 110 hours to index a dataset of 333227 EBSPs using the DI method; but is slower than the SHT methods discussed in the introduction. [25] We also note that the denoising method demonstrated here is agnostic towards its material crystal system, it simply denoises EBSPs, while the DI method becomes increasingly computationally complex with increasing crystal symmetry due to increasing dictionary size. [51], [52]

As denoising was run on the CPU only, computational overhead could be reduced by processing images on the GPU by enabling CUDA support. The DA could also be translated to hardware, at the detector level, in FPGA form for a more energy and computationally efficient implementation. [53], [54] We also must stress that the model was trained with a specific EBSP resolution and detector binning (2x2) in mind, and thus alterations to the model architecture may be necessary for compatibility with patterns collected at higher or lower resolutions. Although EBSP denoising does add computation time following data collection, it does not do so at the point-of-collection or point-of-indexing, and thus could easily be integrated into existing high speed EBSD workflows. When used as EBSD data post-processing, this DA method can enable faster data collection speeds at the detector by allowing collection of noisier EBSPs at lower exposure times. This can help further enable the capture of larger microstructural areas with greater spatial resolution while utilizing conventional Hough-transformation indexing methods.

5.2) Implications of DA post-processing towards HR-EBSD Strain Measurement

As discussed in the introduction, quantifying absolute strain from HR-EBSD pattern cross correlation relies on good convergence between a simulated, zero strain, EBSP and the experimental EBSP. This can be achieved by way of enabling higher accuracy measurement of orientation with DA-processed EBSPs, and with ~36% of the data showing sub-1° of fit, a higher accuracy Hough procedure enables more accurate pattern simulation and absolute strain cross correlation. The improvements to the fit parameter, CI, and orientation indexing observed in Figure 5 translates to a more accurate generation of simulated EBSPs for cross correlation due to increased accuracy of the measured Euler angles, and when combined the enhanced band contrast and edge definition of the DA-processed EBSPs, produces a cross-correlation result with less error and requires less computational iteration to arrive at a solution. This is because uncertainty and error in the Hough indexing procedure carry into the EBSP pattern generation and strain cross correlation procedure, and a poorly indexed experimental point will generate a poorly fit simulated EBSP. Thus, if orientation measurement error can be minimized so to can absolute strain measurement error. [1] As Figure 8 would indicate, increasing the orientation fit accuracy with refined Euler angles does increase correspondence between the simulated zero-strain EBSP and the experimental pattern used to calculate the deformation gradient tensor, while Figure 7.A and B show it is not merely the improved Euler angle fit but that EBSP image quality improvements themselves also drive improvements as well. A combination of the more accurately fit simulated pattern and the DA-improved EBSP image quality is the source of the increased mutual information seen across the datasets in Figure 5.A and this results in reduced 'phantom' or erroneously calculated strains across the entirety of the dataset. As the zero-strain point of cross correlation is more accurately fit, the contributions of phantom strains calculated from erroneous ROI shifts as shown in Figure 8, is reduced, leading to an overall lower average strain. Hence when comparing the strain maps in Figure 7.B and C to D we see more areas of contiguous strain being resolved with less high strain points randomly distributed, as point-to-point misorientation noise is reduced and the patterns have less noise between them. This is why there is significantly higher phantom strains manifested in Figure 7.B, as we are comparing a more accurately simulated pattern to a poorer quality, as-collected image, which results in even greater shift magnitudes between ROIs and a larger perceived deformation gradient. As the strain cross-correlation process is sensitive to high degrees of misorientation between the reference and experimental pattern, a more accurate and correctly fit input orientation map from Hough-indexing results in a better fit zero-strain pattern simulation, and thus reduced ROI shifts and strain magnitude. [1] The reduced number of iterations, and thus time, required to arrive at a cross-correlated strain solution when utilizing the DA-processed patterns and indexing solution could serve to increase the speed of this method, which is the subject of future research.

While the results demonstrate that the DA-processed images are more similar to an idealized simulated EBSP and the improved fit map results in less noise across the strain map with reduced phantom strain contributions relative to the as-collected dataset and patterns, other contributions to phantom strain are not accounted for in this study. The relatively low resolution of the patterns, intentionally poor sample surface preparation, and lack of pattern center (PC) calibration prohibits us from claiming these strain measurements as a ground truth. We recognize contributions from PC error were not addressed, although we argue that achieving such a low absolute strain measurement (.10%) on a heat-treated sample does indicate this contribution is minimal, but without further experimentation cannot quantify this. We note that the sample EBSD area shown is $\sim$.1mm^2 in surface area; and deviations from the as-calibrated PC and the true PC would be expected. [14] We would expect greater strain accuracy and precision utilizing higher resolution EBSPs or with higher resolution EBSD scans taken over a smaller imaging area where less beam shift would be expected, but this requires additional study. Furthermore, no PC recalibration or recalculation occurred in post-processing, and doing so could result in further reductions to phantom strain and improved precision of the local crystal orientation. [55]

Although the improvements to indexing demonstrated by the DA framework shown translates to improved convergence between experimental and simulated patterns, they do not account or correct for PC shift error.

6) Conclusions

The noise limitations of the Hough transformation method of EBSD indexing can be overcome and noisy EBSPs datasets indexed with greater success and accuracy with the use of a denoising autoencoder to process the EBSPs prior to re-indexing. The autoencoder improves indexing quality by improving Kikuchi band contrast and definition, and thus improves IQ, CI, and fit; the neural network learning from noise-free, high contrast, EBSPs to discern high quality image features from noisy ones. Thus, without the introduction of new indexing algorithms, the Hough-transformation indexing process can be improved and made more accurate by denoising the source EBSP prior to indexing. Even with physical dead zones in the detector screen and a poorly polished sample, by combining our DA with existing image processing methods high levels of indexing confidence can be achieved. Both with and without dataset background correction, the denoised EBSPs resulted in a more coherent orientation map with higher CI, IQ, and fit parameters than the as-collected dataset under identical conditions. The ability to index EBSD datasets with greater noise tolerance can allow for faster data collection rates at the detector, enable higher spatial resolution data collection for mesoscale EBSD experiments, and the higher orientation fit accuracy enabled by DA-processing serve to improve the Hough-transform method as a whole.

The improvements made to EBSP quality and subsequent indexing metrics also had implications for cross correlative absolute strain measurement, although there are challenges still present with the method. When using the denoised EBSPs and the higher fit accuracy Euler angles in absolute strain cross correlation, the DA-processed dataset resulted in a more accurate generation of simulated EBSPs from which strain is calculated and required less computational iteration to arrive at a solution. When using the DA-processed EBSPs, there was less apparent misorientation between the experimental pattern and simulated one, which resulted in a reduced ROI shifts necessary to correlate the two patterns and the origin of the reduced phantom strains. Thus, using DA-processed and re-indexed EBSPs offers improvement of correspondence between the experimental and simulated patterns being cross correlated, and much more reliable absolute strain measurements are enabled via HR-EBSD, in addition to improving the indexability of noisy EBSD datasets in general.

Acknowledgements

We would like to thank Dave Rowenhorst at the Naval Research Laboratory for their helpful conversations and insight towards working with ‘.up2’ file structures. Additionally, we would like to thank Jean-Baptiste Forien for their work on the manufacture of these samples and continued support. Portions of this work was performed under the auspices of the Office of Naval Research under contract N00014-20-1-2788. Portions of this work was performed under the auspices of the U.S. Department of Energy by Lawrence Livermore National Laboratory under Contract DE-AC52-07NA27344.

References

[1] D. J. Dingley, G. Meaden, D. J. Dingley, and A. P. Day, "A review of EBSD: From rudimentary on line orientation measurements to high resolution elastic strain measurements over the past 30 years.," *IOP Conf. Ser. Mater. Sci. Eng.*, vol. 375, no. 1, 2018, doi: 10.1088/1757-899X/375/1/012003.

[2] A. J. Schwartz, M. Kumar, B. L. Adams, and D. P. Field, *Electron backscatter diffraction in materials science*. 2009.

[3] T. Ben Britton and J. L. R. Hickey, "Understanding deformation with high angular resolution electron backscatter diffraction (HR-EBSD)," 2017.

[4] A. J. Wilkinson, G. Meaden, and D. J. Dingley, "High resolution mapping of strains and rotations using electron backscatter diffraction," *Mater. Sci. Technol.*, vol. 22, no. 11, pp. 1271–1278, 2006, doi: 10.1179/174328406X130966.

[5] A. J. Wilkinson and T. Ben Britton, "Strains, planes, and EBSD in materials science," *Mater. Today*, vol. 15, no. 9, pp. 366–376, 2012, doi: 10.1016/S1369-7021(12)70163-3.

[6] A. J. Wilkinson, G. Meaden, and D. J. Dingley, "High-resolution elastic strain measurement from electron backscatter diffraction patterns: New levels of sensitivity," *Ultramicroscopy*, vol. 106, no. 4–5, pp. 307–313, 2006, doi: 10.1016/j.ultramic.2005.10.001.

[7] K. Z. Troost, P. Van Der Sluis, and D. J. Gravesteijn, "Microscale elastic-strain determination by backscatter Kikuchi diffraction in the scanning electron microscope," *Appl. Phys. Lett.*, vol. 62, no. 10, pp. 1110–1112, 1993, doi: 10.1063/1.108758.

[8] D. Fullwood, M. Vaudin, C. Daniels, T. Ruggles, and S. I. Wright, "Validation of kinematically simulated pattern HR-EBSD for measuring absolute strains and lattice tetragonality," *Mater. Charact.*, vol. 107, pp. 270–277, 2015, doi: 10.1016/j.matchar.2015.07.017.

[9] P. G. Callahan and M. De Graef, "Dynamical electron backscatter diffraction patterns. Part I: Pattern simulations," *Microsc. Microanal.*, vol. 19, no. 5, pp. 1255–1265, 2013, doi: 10.1017/S1431927613001840.

[10] A. Winkelmann, C. Trager-Cowan, F. Sweeney, A. P. Day, and P. Parbrook, "Many-beam dynamical simulation of electron backscatter diffraction patterns," *Ultramicroscopy*, vol. 107, no. 4–5, pp. 414–421, 2007, doi: 10.1016/j.ultramic.2006.10.006.

[11] T. Tanaka and A. J. Wilkinson, "Pattern matching analysis of electron backscatter diffraction patterns for pattern centre, crystal orientation and absolute elastic strain determination – accuracy and precision assessment," *Ultramicroscopy*, vol. 202, no. April, pp. 87–99, 2019, doi: 10.1016/j.ultramic.2019.04.006.

[12] T. B. Britton *et al.*, "Factors affecting the accuracy of high resolution electron backscatter diffraction when using simulated patterns," *Ultramicroscopy*, vol. 110, no. 12, pp. 1443–1453, 2010, doi: 10.1016/j.ultramic.2010.08.001.

[13] J. Alkorta, M. Marteleur, and P. J. Jacques, "Improved simulation based HR-EBSD

procedure using image gradient based DIC techniques," *Ultramicroscopy*, vol. 182, pp. 17–27, 2017, doi: 10.1016/j.ultramic.2017.06.015.

[14] J. Alkorta, "Limits of simulation based high resolution EBSD," *Ultramicroscopy*, vol. 131, pp. 33–38, 2013, doi: 10.1016/j.ultramic.2013.03.020.

[15] B. L. Adams, S. I. Wright, and K. Kunze, "Orientation imaging: The emergence of a new microscopy," *Metall. Trans. A*, vol. 24, no. 4, pp. 819–831, 1993, doi: 10.1007/BF02656503.

[16] S. I. Wright, M. M. Nowell, R. De Kloe, P. Camus, and T. Rampton, "Electron imaging with an EBSD detector," *Ultramicroscopy*, vol. 148, pp. 132–145, 2015, doi: 10.1016/j.ultramic.2014.10.002.

[17] S. I. Wright, "Review of automated orientation imaging microscopy (OIM)," *J. Comput. Assist. Microsc.*, vol. 5, no. 3, pp. 207–221, 1993.

[18] R. O. Duda and P. E. Hart, "Use of the Hough Transformation to Detect Lines and Curves in Pictures," *Commun. ACM*, vol. 15, no. 1, pp. 11–15, 1972, doi: 10.1145/361237.361242.

[19] S. I. Wright and B. L. Adams, "Automatic analysis of electron backscatter diffraction patterns," *Metall. Trans. A*, vol. 23, no. 3, pp. 759–767, 1992, doi: 10.1007/BF02675553.

[20] AMETEK, "Understanding Electron Backscatter Diffraction (EBSD) Background Corrections." [Online]. Available: https://www.edax.com/-/media/ametekedax/files/resources/tips_tricks/understandingebsdbackgroundcorrections.pdf.

[21] L. T. Hansen *et al.*, "Influence of Noise-Generating Factors on Cross-Correlation Electron Backscatter Diffraction (EBSD) Measurement of Geometrically Necessary Dislocations (GNDs)," *Microsc. Microanal.*, vol. 23, no. 3, pp. 460–471, 2017, doi: 10.1017/S1431927617000204.

[22] P. T. Brewick, S. I. Wright, and D. J. Rowenhorst, "NLPAR: Non-local smoothing for enhanced EBSD pattern indexing," *Ultramicroscopy*, vol. 200, no. December 2018, pp. 50–61, 2019, doi: 10.1016/j.ultramic.2019.02.013.

[23] T. J. Ruggles, T. M. Rampton, A. Khosravani, and D. T. Fullwood, "The effect of length scale on the determination of geometrically necessary dislocations via EBSD continuum dislocation microscopy," *Ultramicroscopy*, vol. 164, pp. 1–10, 2016, doi: 10.1016/j.ultramic.2016.03.003.

[24] S. I. Wright, M. M. Nowell, S. P. Lindeman, P. P. Camus, M. De Graef, and M. A. Jackson, "Introduction and comparison of new EBSD post-processing methodologies," *Ultramicroscopy*, vol. 159, no. P1, pp. 81–94, 2015, doi: 10.1016/j.ultramic.2015.08.001.

[25] W. C. Lenthe, S. Singh, and M. De Graef, "A spherical harmonic transform approach to the indexing of electron back-scattered diffraction patterns," *Ultramicroscopy*, vol. 207, no. September, p. 112841, 2019, doi: 10.1016/j.ultramic.2019.112841.

[26] F. Ram, S. Wright, S. Singh, and M. De Graef, "Error analysis of the crystal orientations

obtained by the dictionary approach to EBSD indexing," *Ultramicroscopy*, vol. 181, pp. 17–26, 2017, doi: 10.1016/j.ultramic.2017.04.016.

[27] S. Singh and M. De Graef, "Orientation sampling for dictionary-based diffraction pattern indexing methods," *Model. Simul. Mater. Sci. Eng.*, vol. 24, no. 8, 2016, doi: 10.1088/0965-0393/24/8/085013.

[28] A. Foden, D. M. Collins, A. J. Wilkinson, and T. B. Britton, "Indexing electron backscatter diffraction patterns with a refined template matching approach," *Ultramicroscopy*, vol. 207, no. September, p. 112845, 2019, doi: 10.1016/j.ultramic.2019.112845.

[29] S. D. Sitzman, G. Nolze, M. M. Nowell, and O. I. America, "EBSD Pattern Quality and its Use in Evaluating Sample Surface Condition," vol. 16, no. Suppl 2, pp. 698–699, 2010, doi: 10.1017/S14319276100.

[30] S. I. Wright and M. M. Nowell, "EBSD Image Quality Mapping," *Microsc. Microanal.*, pp. 72–84, 2006.

[31] P. T. Pinard, M. Lagacé, P. Hovington, and D. Thibault, "An Open-Source Engine for the Processing of Electron Backscatter Patterns : M icroscopy M icroanalysis An Open-Source Engine for the Processing of Electron Backscatter Patterns : EBSD-Image," no. June 2011, 2014, doi: 10.1017/S1431927611000456.

[32] T. Laboratories, "Recent advances in the application of orientation imaging," vol. 67, pp. 1–9, 1997.

[33] EDAXinsight, "Understanding the EDAX Autophase Selection Routine."

[34] N. S. De Vincentis and D. P. Field, "Factors affecting Confidence Index in EBSD analysis," *Ultramicroscopy*, vol. 225, no. January, p. 113269, 2021, doi: 10.1016/j.ultramic.2021.113269.

[35] M. Kamaya *et al.*, "Round robin crystal orientation measurement using EBSD for damage assessment," *Mech. Eng. J.*, vol. 3, no. 3, pp. 16–00077, 2016, doi: https://doi.org/10.1299/mej.16-00077.

[36] K. Kaufmann, H. Lane, X. Liu, and K. S. Vecchio, "Efficient few-shot machine learning for classification of EBSD patterns," *Sci. Rep.*, vol. 11, no. 1, pp. 1–12, 2021, doi: 10.1038/s41598-021-87557-5.

[37] D. Jha *et al.*, "Extracting grain orientations from EBSD patterns of polycrystalline materials using convolutional neural networks," *Microsc. Microanal.*, vol. 24, no. 5, pp. 497–502, 2018, doi: 10.1017/S1431927618015131.

[38] Z. Ding, E. Pascal, and M. De Graef, "Indexing of electron back-scatter diffraction patterns using a convolutional neural network," *Acta Mater.*, vol. 199, pp. 370–382, 2020, doi: 10.1016/j.actamat.2020.08.046.

[39] P. Bulletin and C. Ebsd, "NPAR TM NPAR TM Features and Benefits Improved Indexing Performance through Increased SNR."

[40] I. Goodfellow, Y. Bengio, and A. Courville, *Deep Learning*. MIT Press, 2016.

[41] P. Vincent, H. Larochelle, Y. Bengio, and P. A. Manzagol, "Extracting and composing robust features with denoising autoencoders," *Proc. 25th Int. Conf. Mach. Learn.*, pp. 1096–1103, 2008, doi: 10.1145/1390156.1390294.

[42] J. Xie, L. Xu, and E. Chen, "Image denoising and inpainting with deep neural networks," *Adv. Neural Inf. Process. Syst.*, vol. 1, pp. 341–349, 2012.

[43] L. Gondara, "Medical Image Denoising Using Convolutional Denoising Autoencoders," *IEEE Int. Conf. Data Min. Work. ICDMW*, vol. 0, pp. 241–246, 2016, doi: 10.1109/ICDMW.2016.0041.

[44] W. El-Shafai *et al.*, "Efficient deep-learning-based autoencoder denoising approach for medical image diagnosis," *Comput. Mater. Contin.*, vol. 70, no. 3, pp. 6107–6125, 2022, doi: 10.32604/cmc.2022.020698.

[45] D. Fullwood and H. Lanson, "OpenXY." Salt Lake City, 2015.

[46] M. De Graef *et al.*, "EMsoft." 2019, doi: 10.5281/zenodo.3489720.

[47] D. Joy, *Monte Carlo modelling for electron microscopy and microanalysis*. 1995.

[48] C. E. Andrews, "EBSD Denoising Autoencoder." 2022.

[49] B. E. Jackson *et al.*, "Performance of dynamically simulated reference patterns for cross-correlation electron backscatter diffraction," *Microsc. Microanal.*, vol. 22, no. 4, pp. 789–802, 2016, doi: 10.1017/S143192761601148X.

[50] D. B. Russakoff, C. Tomasi, T. Rohlfing, and C. R. Maurer, "Image Similarity Using Mutual Information of Regions," pp. 596–607, 2004.

[51] Y. H. Chen *et al.*, "A Dictionary Approach to Electron Backscatter Diffraction Indexing," *Microsc. Microanal.*, vol. 21, no. 3, pp. 739–752, 2015, doi: 10.1017/S1431927615000756.

[52] M. De Graef, "A dictionary indexing approach for EBSD," 2020, doi: doi:10.1088/1757-899X/891/1/012009.

[53] Altera, "Efficient Implementation of Neural Network Systems Built on FPGAs, Programmed with OpenCL," p. 2, 2016.

[54] Y. Hao, "A General Neural Network Hardware Architecture on FPGA," 2017, [Online]. Available: http://arxiv.org/abs/1711.05860.

[55] Q. Shi *et al.*, "Calibration of crystal orientation and pattern center of EBSD using integrated digital image correlation," *Mater. Charact.*, vol. 178, no. May, 2021, doi: 10.1016/j.matchar.2021.111206.